Design rules for frequency conversion in periodically poled lithium niobate-on-insulator waveguides

Yesim Koyaz[a], Christian Lafforgue[a], Nikolay Balakleyskiy[a], Olivia Hefti[a,b], Homa Zarebidaki[b], Amir Ghadimi[b], Hamed Sattari[b], Davide Grassani[b], and Camille-Sophie Brès[a]

[a]Ecole Polytechnique Fédérale de Lausanne, Photonic Systems Laboratory (PHOSL), STI-IEM, Station 11, CH-1015 Lausanne, Switzerland
[b]CSEM Neuchâtel, Rue Jaquet-Droz 1, 2002 Neuchâtel, Switzerland

ABSTRACT

The rapid development of photonic applications calls for scalable, miniaturized power efficient integrated circuits. Thin film lithium niobate (TFLN) now emerges as a major photonic platform for integration of advanced functionalities such as based on nonlinear optics. We report experimentally efficient second harmonic generation in periodically poled lithium niobate waveguides and design rules for nonlinear frequency conversion, including a study on tolerances on the dimensions and poling parameters. Our work aims at establishing reliable and versatile nonlinear building blocks for scalable TFLN photonic integrated circuits.

Keywords: Second-harmonic generation, nonlinear frequency conversion, periodically poled waveguides, thin-film lithium niobate, photonic integrated circuit, nonlinear optics

1. INTRODUCTION

Lithium niobate has been commercially used in optoelectronics for many decades. It is particularly favorable because of its high second-order nonlinearity and wide transparency window that extends from near-UV to mid-IR.[1,2,3] Thanks to the recent advances on microfabrication, thin-film lithium niobate (TFLN) can be now directly patterned in the form of waveguides on top of silica BOX, enabling strongly guided light throughout the device.[4,5] The propagation loss in patterned TFLN waveguides are reported to be less than <0.1dB/cm in state-of-the-art devices.[6,7,8] In addition to its electro-optic properties, high nonlinearity, both of the second and third order, combined with low-loss promises a superior photonic integrated circuit (PIC) platform capable of providing high-efficiency nonlinear frequency generation. In this work, second order three-wave mixing processes, in particular second-harmonic generation (SHG), and its tolerance margin with respect to fabrication fluctuations are studied in TFLN waveguides.

TFLN stands out among different platforms for the ease of periodic poling thanks to lithium niobate's ferroelectric properties. To periodically pole TFLN, high voltage millisecond pulses are applied from patterned electrodes to generate electric field parallel to the extraordinary axes. As a result of this electric field, the direction of the effective second order susceptibility ($\chi^{(2)}$) will be flipped periodically, to facilitate quasi-phase matching (QPM). By solely engineering the poling period, QPM requirements for different three-wave mixing processes can be fulfilled within the selected waveguide cross-section of the TFLN platform.

In this work, we performed mode simulations to calculate SHG poling period, conversion efficiency and bandwidth. We provided design rules for different waveguide cross-sections(where all investigated cross-sections are possible to fabricate upon request) and we pinpointed advantageous waveguide dimensions for narrowband and broadband operation. Given possible fluctuations in fabrication, we also performed a tolerance analysis on waveguide dimensions, which is critical in view of fabricating devices with guaranteed performances. We confirmed our calculations with SHG measurements.

Corresponding author: camille.bres@epfl.ch

2. RESULTS

We calculated the mode distribution and transverse electric field for pump wavelengths from 1.5 μm to 1.6 μm and for second harmonic (SH) wavelengths from 0.775 μm to 0.8 μm by using a numerical solver.

As the performance metric, on-chip SHG conversion efficiency (CE) is used in our theoretical analysis and it is expressed as:

$$P_h(z) = CE(z) \times P_p(z)^2 \tag{1}$$

where P_h and P_p are the harmonic and pump powers respectively, and z is the propagation distance.

CE is calculated for periodically poled waveguides with 50% duty cycle and complete domain inversion by using Eq. 2:

$$CE(z) = \frac{4}{\pi^2} \left|\gamma_{SH}\right|^2 z^2 \operatorname{sinc}\left(\frac{\Delta\beta}{2}z\right)^2 \tag{2}$$

where $\left|\gamma_{SH}\right|^2$, $\Delta\beta$, z are nonlinear mode overlap, phase mismatch and the length of the periodically poled section respectively.

The nonlinear mode overlap, $\left|\gamma_{SH}\right|^2$, that includes the modes' distribution, is defined as [9]:

$$\left|\gamma_{SH}\right|^2 = \frac{\omega_p^2 \left(\chi^{(2)}\right)^2}{2\varepsilon_o c^3 n_{eff,p}^2 n_{eff,h}} \frac{\left(\iint E_p^*(x,y)^2 E_h(x,y)dxdy\right)^2}{\left(\iint |E_p(x,y)|^2 dxdy\right)^2 \iint |E_h(x,y)|^2 dxdy} \tag{3}$$

where $n_{eff,h/p}$, ω_p and E_h/p is the effective index of SH/pump, pump angular frequency and the electric field of SH/pump on each position respectively.

Phase mismatch, $\Delta\beta$, is composed from intrinsic phase mismatch, $\Delta\beta_0$, and poling period, Λ:

$$\Delta\beta = \Delta\beta_0 - \frac{2\pi}{\Lambda} \text{ and } \Delta\beta_0 = \frac{2\pi}{\lambda_p/2}\left(n_{eff,h} - n_{eff,p}\right) \tag{4}$$

where $n_{eff,h/p}$, λ_p is the effective index of SH/pump and pump wavelength, respectively.
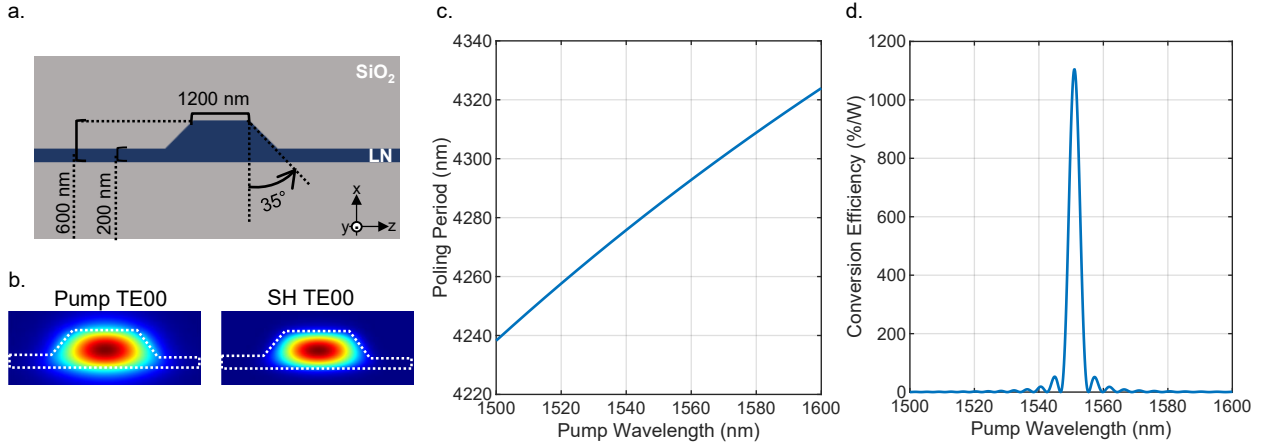

Figure 1. a) Schematic of of a possible cross section where waveguide dimensions and lithium niobate coordinate axes are labelled. b) Mode profiles of fundamental TE mode of pump (1.55 μm) and SH (775 nm). c) Poling period calculated for quasi-phase matched SHG while sweeping pump wavelength from 1500 nm to 1600 nm and d) Quasi-phase matched conversion efficiency when the poling duty cycle is 50% and poling period is selected to optimize ~1550 nm operation for the cross-section presented in (a).

Poling period, Λ, is selected to compensate $\Delta\beta_0$ at the desired wavelength. As a result, it is calculated with Eq. 5:

$$\Lambda = \frac{\lambda_p}{2(n_{eff,h} - n_{eff,p})} \tag{5}$$

Then, by using Eq. 1-5, we calculated poling period, theoretical CE for a range of possible waveguide cross-sections. In Fig. 1, one of such cross-sections and results are presented. Our analysis focuses on fundamental TE mode of pump and SH to work with highest effective $\chi^{(2)}$ (Fig. 1b). For this cross-section, at 1550 nm pump incidence, the calculated poling period is 4257 nm, maximum value of CE is 1122 %/W and its bandwidth is $\sim$4 nm for the PPLN length of 5 mm.

The analysis covers waveguide ridge widths upto 1800 nm, while keeping the same standard film thickness and etch depth, for cladded (with SiO_2)(Fig. 2a-b) and for uncladded (without SiO_2)(Fig. 2d-e) waveguides. The 2D-sweeps show the maximum CE which corresponds to CE at the quasi-phase matched pump wavelength (Fig. 2a-d) and the bandwidth which corresponds to FWHM of CE (Fig. 2b-e). The maps indicate that the largest bandwidth is at uncladded waveguide width of $\sim$600 nm. All in all, we observe that the bandwidth is narrower at shorter pump wavelengths and CE is lower at wider waveguides.

According to the numerical simulations, it is important to note that the waveguide widths from 700 nm to 900 nm are not preferable to generate SH at fundamental TE mode on the cladded configuration (likewise within waveguide widths from 700 nm to 1000 nm on the uncladded configuration) . Within this region, the simulations indicate that the fundamental SH mode is hybridized and has both TE and TM contributions. We include the waveguide widths that has a TM contribution higher than 5% to the hybrid mode region. This region is also labelled on Fig. 2. The presence of hybridization is also reported in literature.[10,11] For the calculations of bandwidth and CE, we only take the TE component into account.

We are interested in designs for both narrowband and broadband operation. In Fig. 2c&f, favorable cross-sections for narrowband and broadband operation are shown. For narrowband operation, the cladded waveguide with waveguide ridge width of 400 nm and length of 10 mm is the most preferable. In this waveguide, calculated bandwidth is $\sim$1.4 nm provided that the poling period is adjusted to have the SH-peak at $\sim$1550 nm. For broadband operation, we pinpoint the uncladded waveguide with ridge width of 600nm and length of 5 mm to achieve a bandwidth around $\sim$10 nm.

The analysis up to now (Fig. 1 and Fig. 2) assumes that poling period compensates $\Delta\beta$ at the designed frequency and SH peak is observed at the intended wavelength. However, in measurements, SH-peak position may shift from the designed value. We quantify this shift by extending numerical simulations to all possible waveguide cross-sections that lie within the tolerance limits of fabrication for etch depth, ridge width and etch angle. These deviations from the designed waveguide cross-section will alter the poling period and consequently cause a shift on SH-peak. We performed the tolerance on the same cross-section presented on Fig. 1a.

For 30 nm smaller ridge width, $\sim$25 nm shift on poling period is foreseen as shown in Fig. 3a. Similarly, 30 nm shift on etch depth, is likely to correspond to $\sim$17 nm shift on poling period (Fig. 3b) and 3°variation on etch angle, can cause $\sim$28 nm shift poling period (Fig. 3c). Summing up all deviations, the actual poling period can shift $\pm$70 nm from the intended design. This also implies that the deviations on waveguide cross-section can shift poling period as much as 140 nm between two fabrication rounds. As 40 nm deviation from the designed poling period may cause $\sim$48 nm shift on SH peak, fabrication tolerances should be taken into account while generating SHG building blocks within periodically poled TFLN platform.

We performed optical measurements to validate our analysis. The waveguides are fabricated in CSEM and their design cross-section is given in Fig. 1a. In the measurement setup(Fig. 3a-inset), a wavelength tunable laser is used and light is coupled through a lensed fiber. The chip is placed on a temperature controlled Peltier stage at its temperature is kept constant on 21°. At the output, an objective collects the outcoupled light and pump and SH signals are detected simultaneously. A wavelength dependent dichroic mirror/beamsplitter is used to direct each to a different powermeters. Out-coupled conversion efficiency (CE) is obtained by dividing SH power reading to squared pump power reading. We measured out-coupled conversion efficiency as high as $\sim$600 %/W. By taking coupling losses of pump and SH into account, on-chip conversion efficiency is estimated to be >150 %/W where the length of PPLN is 4.8 mm.
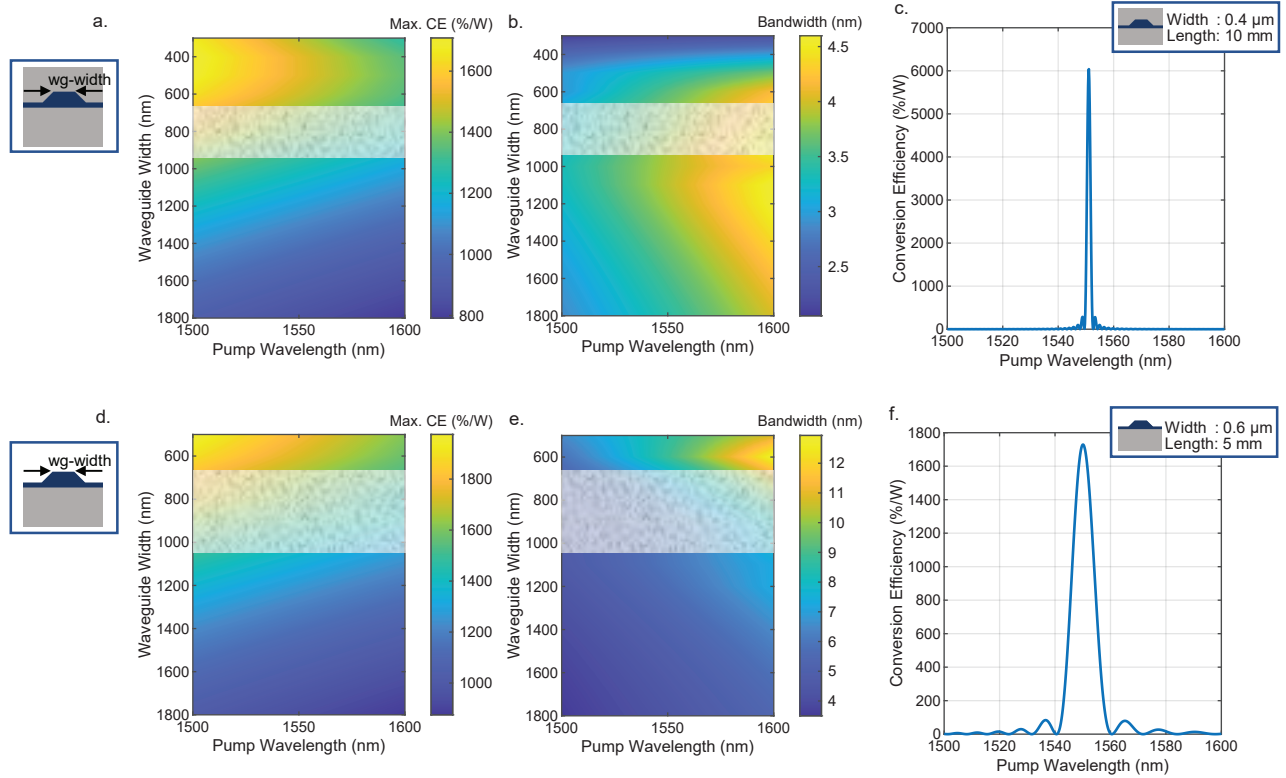
3

Figure 2. Simulations for different waveguide widths with lithium niobate film thickness of 600 nm, etch depth of 400 nm and periodically-poled waveguide length of 5 mm. Hybrid mode region is labelled in grey. a,d) Peak value of CE for a) cladded and d) uncladded cross-sections, and b,e) Bandwidth of CE for b) cladded and e) uncladded cross-sections. c,f) Pinpointed cross-sections for c) narrowband operation with bandwidth of ∼1.4 nm and f) broadband operation with bandwidth of ∼10 nm where QPM period is selected to have the SH-peak at ∼1550 nm.

Normalized CE for different PPLN waveguides are showed in Fig. 3d. We compared different fabrication rounds (by using waveguides on different wafers - WF). We also compared different poling periods (namely poling period 4200 nm and 4300) and two different waveguides with the same poling period where these waveguides are all located on the same wafer (WFA). We associate the deviations from the sinc-squared CE form with poling imperfections. In Fig. 3a, scattered data points corresponds to one-to-one division of pump and SH-readings. As there has been an additional wavelength dependent oscillation present on solely pump readings, we also plotted CE by using the envelope of the pump readings and it is shown with solid lines.

Via these measurements, first, we compare waveguides with the same poling period (4200 nm) but originally from different wafers(WG1, located on WFA, and WG6, located on WFC). SH-peak is observed at ∼1534 nm in WG1 and ∼1590 nm in WG6. The difference on SH-peak position lies within the range we predicted within the tolerances analysis. In addition, we characterize another waveguide (WG5, located on WFB) from a different Wafer with the poling period of 4100 nm. Its SH-peak is measured at ∼1592 nm which lies in the same region that we observed the SH-peak of WG6. Hence, we experimentally show the shift on poling period as high as 100 nm between different wafers.

We also quantified the shift of SH-peak for different poling periods namely 4200 nm (WG1) and 4300 nm (WG4) for the waveguides from the same wafer (WF-A). For these waveguides, SH-peak is observed at ∼1534 nm and ∼1642 nm respectively. In simulations, for the design cross-section, SH-peak is at ∼1490 nm when QPM period is 4200 nm and it shifts ∼116 nm when QPM period shifts ∼100nm. Therefore, it is seen that the experimental shift of SH-peak is in agreement with the simulations.
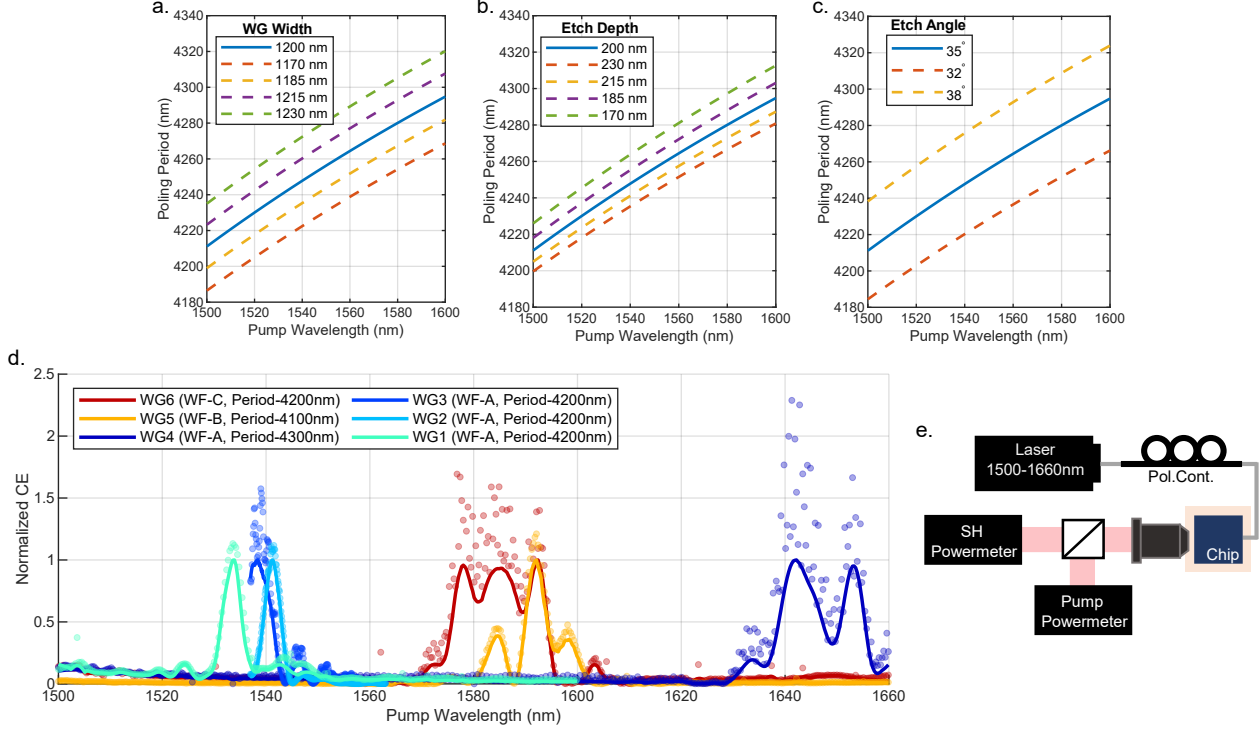
4

Figure 3. a-c) Poling period versus pump wavelength plots to quantify the effect of fabrication deviations in the poling period. a) Waveguide width sweep for the error range of ±30 nm when targeted waveguide width is 1200 nm. b) Etch depth sweep for the error range of ±30 nm when targeted etch depth is 200 nm. c) Etch angle sweep for the error range of ±3° when targeted etch depth is 35°. d) Normalized outcoupled SHG conversion efficiency (CE) for different periodically poled waveguides from different wafers(WF). e) SHG characterization setup where Peltier stage temperature is at 21°. For WFA-WG2&3, an amplifier and polarization filter are added to the beam path and stage temperature is 55°.

In addition, we compared two waveguides from the same wafer and has the same QPM period (4200 nm). These waveguides, namely WG2 and WG3, are measured within the same setup but by pumping higher input power from a C-band amplifier, passing through an isolator and by heating the Peltier stage to 55°(instead of 21°) so that the SH-peak lies within amplifier's wavelength range. The shift on SH-peak between WG2 and WG3 is ∼3 nm. It is indeed significantly smaller than the shift we observed between different wafers.

Considering the relative shift on SH-peak between the waveguides, our experimental results are in accordance with the theoretical expectations. However, the absolute value of the SH-peak position is shifted to longer wavelengths on all measured waveguides. One reason for this discrepancy could be due material dispersion data. Current analysis uses theoretical refractive index values for lithium niobate[12] and the calculated values could be improved by using dispersion data from ellipsometry measurements.

3. DISCUSSION AND CONCLUSION

In conclusion, we provided the design rules for SHG for different waveguide widths (upto 1800 nm) through the pump wavelength range from 1.5 μm to 1.6 μm. We proposed the favorable cross-sections for narrowband (∼1.4 nm) and broadband (∼10 nm) operation. We performed a tolerance analysis for fabrication deviations, namely waveguide width, etch depth and etch angle and we show that a possible shift on poling period as high as ±70 nm is expected from the designed value. We also measured SH on different waveguides and experimentally verify the theoretical analysis. As the next step, we are working on extending the analysis for the design rules for different three-wave mixing processes, namely difference-frequency generation, with the motivation of extending the operation to mid-IR wavelengths.

Our results show the sensitivity of operation to poling period and fabricated waveguide cross-section. Additional methods are required to precisely control SH-peak position even within the presence of fabrication deviations. Further tuning of the SH-peak can be achieved by temperature tuning or by precise engineering of the poling period. Yet, our analysis demonstrate by precisely controlling waveguide cross-section, TFLN can provide different design parameters for wide range of applications and therefore, it becomes a strong candidate to form standardized PIC platform on nonlinear optics.

ACKNOWLEDGMENTS

REFERENCES

[1] Zhu, D., Shao, L., Yu, M., Cheng, R., Desiatov, B., Xin, C. J., Hu, Y., Holzgrafe, J., Ghosh, S., Shams-Ansari, A., Puma, E., Sinclair, N., Sinclair, N., Reimer, C., Zhang, M., Lončar, M., and Lončar, M., "Integrated photonics on thin-film lithium niobate," *Advances in Optics and Photonics, Vol. 13, Issue 2, pp. 242-352* **13**, 242–352 (6 2021).

[2] Wang, C., Zhang, M., and Lončar, M., "High-Q Lithium Niobate Microcavities and Their Applications," (2020).

[3] Leidinger, M., Fieberg, S., Waasem, N., Kühnemann, F., Buse, K., and Breunig, I., "Comparative study on three highly sensitive absorption measurement techniques characterizing lithium niobate over its entire transparent spectral range," *Optics Express, Vol. 23, Issue 17, pp. 21690-21705* **23**, 21690–21705 (8 2015).

[4] Siew, S. Y., Cheung, E. J. H., Liang, H., Bettiol, A., Toyoda, N., Alshehri, B., Dogheche, E., and Danner, A. J., "Ultra-low loss ridge waveguides on lithium niobate via argon ion milling and gas clustered ion beam smoothening," *Optics Express, Vol. 26, Issue 4, pp. 4421-4430* **26**, 4421–4430 (2 2018).

[5] Wang, C., Xiong, X., Andrade, N., Venkataraman, V., Ren, X.-f., Guo, G.-c., and Lončar, M., "Second harmonic generation in nano-structured thin-film lithium niobate waveguides," *Optics Express, Vol. 25, Issue 6, pp. 6963-6973* **25**, 6963–6973 (3 2017).

[6] Wu, R., Wang, M., Xu, J., Qi, J., Chu, W., Fang, Z., Zhang, J., Zhou, J., Qiao, L., Chai, Z., Lin, J., and Cheng, Y., "Long Low-Loss-Litium Niobate on Insulator Waveguides with Sub-Nanometer Surface Roughness," *Nanomaterials* **8** (11 2018).

[7] Wang, C., Zhang, M., Yu, M., Zhu, R., Hu, H., and Loncar, M., "Monolithic lithium niobate photonic circuits for Kerr frequency comb generation and modulation," *Nature Communications 2019 10:1* **10**, 1–6 (2 2019).

[8] Jankowski, M., Langrock, C., Desiatov, B., Marandi, A., Wang, C., Zhang, M., Phillips, C. R., Lončar, M., and Fejer, M. M., "Ultrabroadband nonlinear optics in nanophotonic periodically poled lithium niobate waveguides," *Optica, Vol. 7, Issue 1, pp. 40-46* **7**, 40–46 (1 2020).

[9] Suhara, T. and Fujimura, M., "Waveguide Nonlinear-Optic Devices," **11** (2003).

[10] Wang, J., Chen, P., Dai, D., and Liu, L., "Polarization Coupling of X Polarization Coupling of X-Cut Thin Film LN Based Waveguides," *IEEE Photonics Journal* **12** (6 2020).

[11] Kaushalram, A., Hegde, G., and Talabattula, S., "Mode hybridization analysis in thin film lithium niobate strip multimode waveguides," *Scientific Reports 2020 10:1* **10**, 1–13 (10 2020).

[12] Zelmon, D. E., Small, D. L., and Jundt, D., "Infrared corrected Sellmeier coefficients for congruently grown lithium niobate and 5 mol.% magnesium oxide–doped lithium niobate," *JOSA B, Vol. 14, Issue 12, pp. 3319-3322* **14**, 3319–3322 (12 1997).